Dalton Transactions

ROYAL SOCIETY OF CHEMISTRY

PAPER

View Article Online
View Journal | View Issue

Cite this: *Dalton Trans.*, 2025, **54**, 14728

Butterfly-like photo-responsive cyclometalated Ir(III) complex: emergence of a future cancer therapeutic agent

Sreelekha U,†[a] Rishav Das,†[a] Indrani Paramasivan Latha Laxmi,[a] Nilmadhab Roy,[a] Riona Roy,[a] Logesh Mathivathanan,[a] Tamizhselvi Ramasamy,[a] Rinku Chakrabarty *[b] and Priyankar Paira *[a]

Received 17th May 2025,
Accepted 26th August 2025

DOI: 10.1039/d5dt01164g

rsc.li/dalton

Herein, we report photoinduced 2,2′-bipyrimidine-based mono- and binuclear cyclometalated iridium(III) complexes as a future promising anticancer agent, exhibiting the best efficiency as type I and type II PDT agents, respectively. The bimetallic complex **IIr$_2$** exhibits superior efficacy in normoxic (type II) and hypoxic (type I) tumour conditions, while the monometallic complex **IIr** is mainly active under normoxic conditions. This enhanced versatility makes **IIr$_2$** a highly promising candidate for photodynamic therapy. The complexes exhibited high serum albumin binding affinity (K_{HSA} = 0.57 × 10^5 M^{-1} for **IIr** and 0.59 × 10^5 M^{-1} for **IIr$_2$**), highlighting their significant potential for biomolecular interactions. Under specific light irradiation, these complexes deplete glutathione levels, proving their efficacy as photodynamic therapeutic agents in future. Among the two synthesized complexes, **IIr$_2$** showed significant phototoxicity against the TNBC cell line (MDA-MB-231), exhibiting an IC_{50} value of 13.6 ± 0.06 μM (PI = 9.9), highlighting its potential as an effective PDT agent.

1. Introduction

Cancer is considered the second most fatal disease worldwide. It is worth noting that the cancer spectrum is expanding due to the rise in cancer cases. Triple negative breast cancer (TNBC) is associated with the worst prognosis, primarily because it lacks the estrogen receptor (ER), progesterone receptor (PR), and human epidermal growth factor receptor 2 (HER2), resulting in limited options for targeted therapies. Despite the significant results achieved by common platinum-based drugs, which are one of the important cornerstones of the cancer treatment process, the development of new drugs is a thrust area of research due to their adverse side effects and significant acquired drug resistance. Their specificity towards targeted cancer cells and limited effectiveness are also matters of concern. Photodynamic therapy is a crucial treatment option that is more targeted and specialised than traditional cancer therapeutic modalities. Upon photoexcitation, a photosensitizer generates reactive oxygen species (ROS) through two mechanisms: type I PDT, involving electron transfer, and type II PDT, involving energy transfer; while the former can function effectively in hypoxic and normoxic situations, the latter is most effective in normoxic conditions. Recently, there has been growing interest in the synthesis of iridium(III) complexes owing to their remarkable photoluminescent properties, high photostability, and large Stokes shift, which collectively make them promising candidates for phototherapeutic applications.[1,2] In iridium(III) complexes, the long-lived triplet excited state resulting from fast intersystem crossing, attributed to the strong spin–orbit coupling (SOC) (ζ_{SOC} = 3909 cm^{-1}) arising from the heavy atom effect of the iridium center, plays a crucial role in facilitating electron transfer (type I PDT) and energy transfer (type II PDT) processes.[3] Cyclometalated Ir(III) complexes are one of the best possible alternatives to combat this perilous disease, which may quench researchers' thirst for developing effective and specific cancer preventive drugs in the future. Cyclometalated Ir(III) complexes are mitochondria-specific and can target cisplatin-resistant cancer cells.[4,5] Ligand selection is a key factor in the design of photoactivated chemotherapeutic agents, with 2,2′-bipyrimidine emerging as a particularly suitable candidate for anticancer applications. Its ability to bind in bidentate or bridging bis-bidentate modes has made 2,2′-bipyrimidine a useful bridging ligand for the creation of homo-dinuclear and hetero-dinuclear complexes for cancer therapy.[6–8] Incorporation of 2,2′-bipyrimidine, functioning as an N^N bidentate ligand, with its planar structure facilitates DNA intercalation and enables targeted delivery. Additionally, it promotes efficient ROS (particularly $^1O_2$) generation by extending the lifetime of the triplet state.[9,10]

[a]*Department of Chemistry, School of Advanced Sciences, Vellore Institute of Technology, Vellore-632014, Tamil Nadu, India. E-mail: priyankar.paira@vit.ac.in*
[b]*Department of Chemistry, Alipurduar University, Alipurduar-736122, West Bengal, India. E-mail: rinkuapduchem@gmail.com*
† These authors contributed equally to this work.

A significant enhancement in the anti-cancer activity of the targeted complex with a binuclear metal core is anticipated, due to the combination of the biological activities of both the ligand and the metal centre.[11] The use of this method will result in high energy efficiency, minimal waste, high atom economy, and an environmentally friendly process.[12] Additionally, the synthesized complexes will undergo characterization and analysis using spectroscopic techniques and biochemical assays to evaluate their potential applications in biology.[13]

2. Results and discussion

Design and synthesis

Over the last few decades, several research groups have shown keen interest in iridium complexes, which act as chemotherapeutic agents through the PDT mechanism.[14–17] Herein, we have designed and synthesized photo-active cyclometalated iridium(III) binuclear complex (Fig. 1).

Scheme 1 delineates the synthetic scheme of the ligand and complexes. The cyclometalated bimetallic Ir(III) precursor (**L**) was synthesized from 2-phenylpyridine as the starting material, following the previously reported literature.[18] The precursor **L** was further reacted with bipyrimidine (1 : 2) to form the monometallic complex **LIr**, whereas the desired bimetallic Ir(III) complex (**LIr$_2$**) was obtained in an excellent yield by changing the ratio of the starting materials (1 : 1). These two complexes were fully characterized by different spectroscopic techniques such as ^{1}H NMR, ^{13}C NMR, FT-IR and HRMS (Fig. S1–S11).

Characterization

In the complex **LIr**, the peak corresponding to the most downfield proton adjacent to the nitrogen in the bipyrimidine ring is observed in the ^{1}H NMR spectrum (δ 9.31–9.33); however, its disappearance in the spectrum of **LIr$_2$** indicates coordination at this site, confirming the formation of **LIr$_2$**. The peaks in the HRMS spectrum at m/z 659.1521 $[M]^+$ and 580.1329 $[M]^{2+}$ confirmed the formation of the complexes **LIr** and **LIr$_2$**, respectively. Purity of both the complexes was verified using high-performance liquid chromatography (HPLC), in which a single peak was observed with purity >95% (Fig. S12 and S13). Crystals suitable for single-crystal X-ray crystallographic analysis were grown from the slow evaporation of a hexane–diethyl ether mixture (Fig. 2). The compound **LIr$_2$** crystallizes in the tetragonal space group $I41/a$ with one-half of the molecule in the asymmetric unit. The crystal lattice contains solvent-accessible voids of about 3400 Å^3. These voids are occupied by disordered diethyl ether and water molecules (Tables T1–T3). Charge from the two Ir^{3+} centers is balanced by the ligand and two chloride ions. The asymmetric unit contains one chloride ion, which was identified and labelled from the difference map.

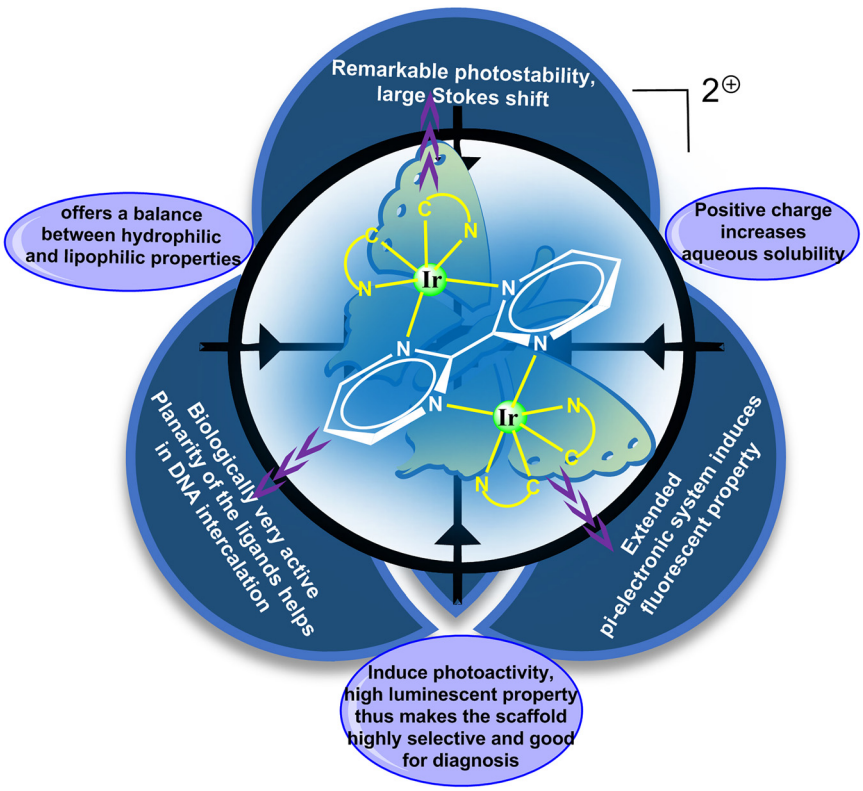

Fig. 1 Design of the bipyrimidine-based cyclometalated iridium(III) complex.

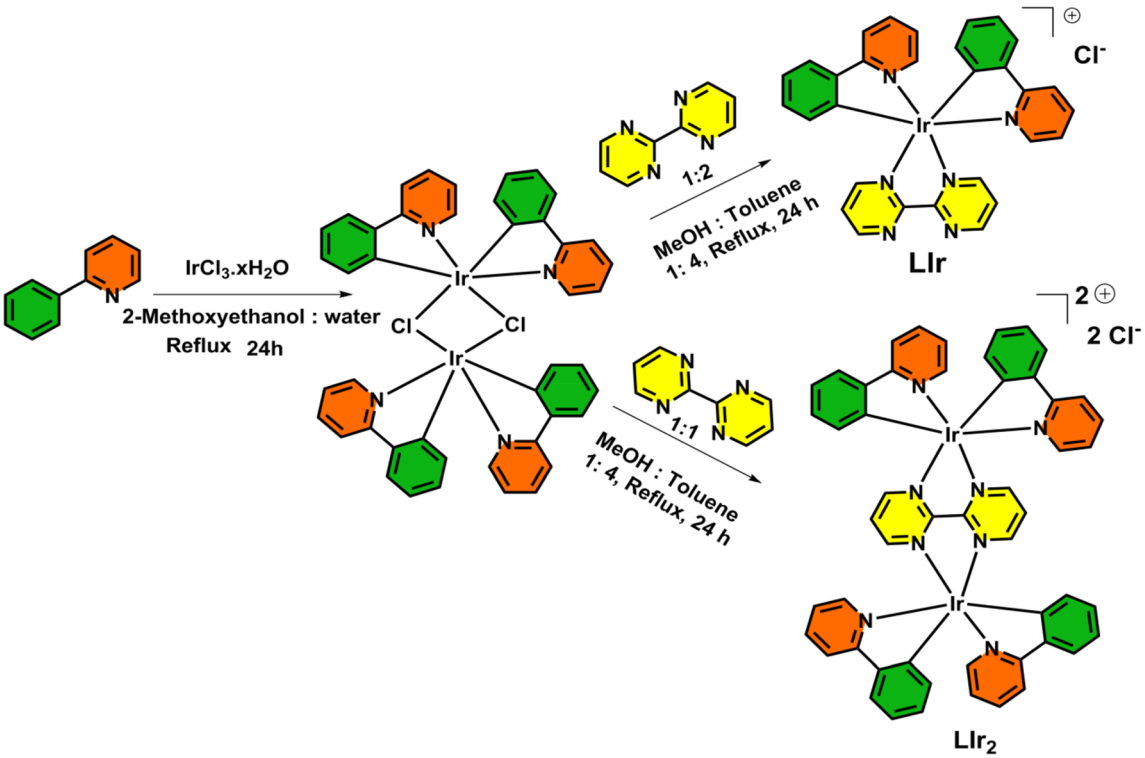

Scheme 1 Synthetic route for the complexes **LIr** and **LIr$_2$**.

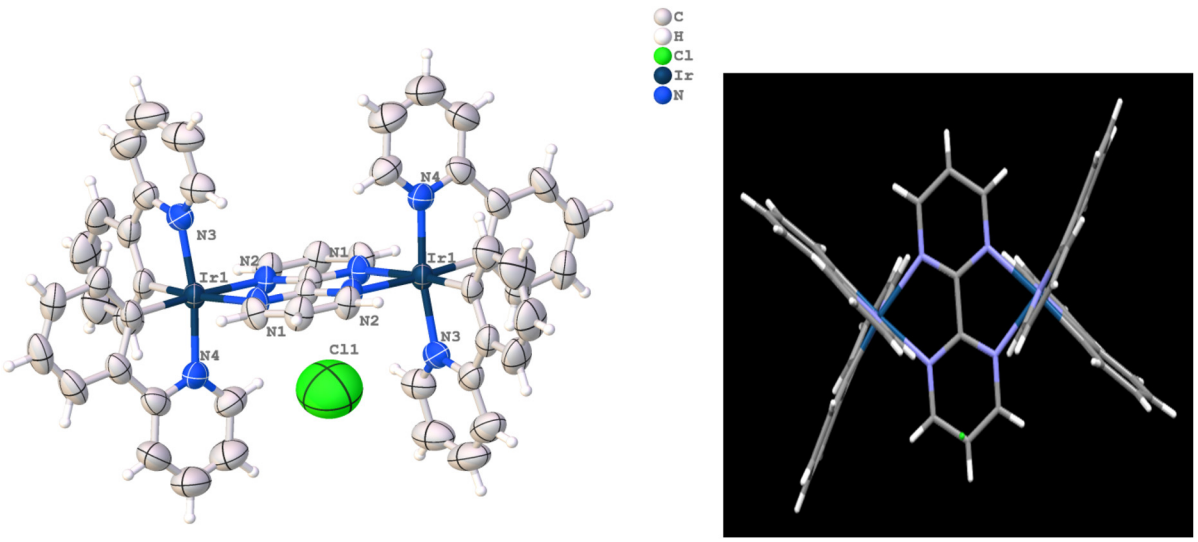

Fig. 2 ORTEP diagram of the butterfly-like X-ray crystal structure of the Ir(III) complex **LIr$_2$** (CCDC 2446109), with thermal ellipsoids drawn at the 50% probability level.

X-ray crystallography

Photophysical studies

UV-Vis and fluorescence studies. Photophysical properties play an important role in designing phototherapeutic agents or metallodrugs for cancer therapy applications. Photo-responsive properties of the synthesized complexes were verified using UV-Vis spectroscopy. In the UV-Vis spectra, spin-allowed π–π* transition bands appear below 350 nm for both the Ir(III) complexes, **LIr** and **LIr$_2$**,[19,20] whereas the moderately intense band from 350 to 450 nm could be assigned to LL′CT (CN → NN) transition (Fig. S14). The less intense absorption at 470 nm for both complexes could be due to the spin-forbidden, mixed singlet and triplet metal-to-ligand and ligand-to-ligand tran-

sitions (^{3}ML′CT/^{3}LL′CT). The emission spectra of complexes **LIr** and **LIr$_2$** displayed emission in the range of 485 nm to 750 nm upon excitation at 470 nm, with a large Stokes shift (>100 nm) attributed to their extended conjugated structure (Fig. S15). Using Rhodamine B in water (Φ = 0.31) as a reference standard, the fluorescence quantum yields of complexes **LIr** and **LIr$_2$** were determined to be 0.46 (in acetonitrile) and 0.33 (in acetonitrile), respectively. The **LIr** exhibited a fluorescence lifetime of 5.3 ns, and the corresponding radiative and non-radiative rate constants were calculated as 8.67×10^7 s^{-1} (K_r) and 1.02×10^8 s^{-1} (K_{nr}), respectively. Similarly, complex **LIr$_2$** exhibited a fluorescence lifetime of 6.5 ns, and its radiative and non-radiative rate constants were determined to be 5.05×10^7 s^{-1} and 1.02×10^8 s^{-1}, respectively (Fig. 3). Higher k_{nr} value favours fast and efficient intersystem crossing (ISC) to an excited triplet state (a non-radiative transition), followed by enhanced ROS generation.

Solubility and stability study

Envisioning solubility and stability of the metallopharmaceuticals in dark and light irradiated conditions is very crucial as it provides insight into the stability of the metallodrugs in various cellular environments and durability under light irradiated conditions within the cells under consideration. To determine the potency of the synthesized metal complexes as therapeutic agents, we evaluated their stability in 10% DMSO and in 1 mM GSH medium over a period of 24 h at 37 °C using the UV-Vis spectroscopic technique (Fig. S16). The complexes **LIr** and **LIr$_2$** demonstrated good photostability when exposed to light for 4 hours in 1 mM GSH and PBS medium, as confirmed by UV-Vis spectroscopy (Fig. S17). Additionally, both complexes remained photostable in a DMSO–methanol mixture, as evidenced by high-resolution mass spectrometry (HRMS) analysis (Fig. 4).

Lipophilicity study

Cell permeability is a characteristic feature of a drug molecule that determines the distribution of the drug after penetrating through the cell membrane. The drug molecules must be capable enough to pass through the gastrointestinal tract and being absorbed into the phospholipid layer of the cell membrane. It is also worth noting that the best intracellular interaction has been observed for the drug molecules possessing a balance between hydrophobicity and lipophilicity. The synthesised complexes **LIr** and **LIr$_2$** exhibited a balanced lipophilic and hydrophilic character (Fig. S26 and S27), which is an essential criterion for the metal complexes to exert antitumour potency. **LIr** is more soluble in an aqueous medium when compared with octanol ($\log P_{o/w} = -1.46865$), while **LIr$_2$** has succeeded in maintaining the equilibrium between both water and octanol ($\log P_{o/w} = -0.25656$), which may facilitate better cellular membrane permeability, and ultimately improve the cellular uptake.

DNA binding study

By UV-Vis method. The potential binding affinity of the Ir(III) complexes with CT-DNA, extracted from calf thymus, was studied using UV-Vis spectroscopic technique (Fig. S18). Hyperchromicity in the UV-Vis spectra with the increasing concentration of CT-DNA, while keeping the concentration of the complexes constant, indicates a non-covalent electrostatic binding or groove-binding mechanism between the CT-DNA and iridium complexes. Benesi–Hildebrand method was applied for the calculation of K_b values (eqn (ii)), which were found to be 6.29×10^3 and 1.19×10^4 M^{-1} for **LIr** and **LIr$_2$**, respectively (Fig. S19).

Ethidium bromide (EtBr) displacement assay

Generally, the degree of intercalation of the complexes with DNA was examined using the fluorescence spectroscopy through an EtBr displacement study.[21] Ethidium bromide (EtBr) is a reagent that binds strongly with DNA and emits strong fluorescence, which decreases after the binding of metal complexes. CT-DNA-bound EtBr solution exhibits strong fluorescence at 591 nm (λ_{ex} = 485 nm) (Fig. S20). The decrease in fluorescence spectra after the addition of **LIr** and **LIr$_2$** proves the strong binding nature of the two (eqn (iii)). The

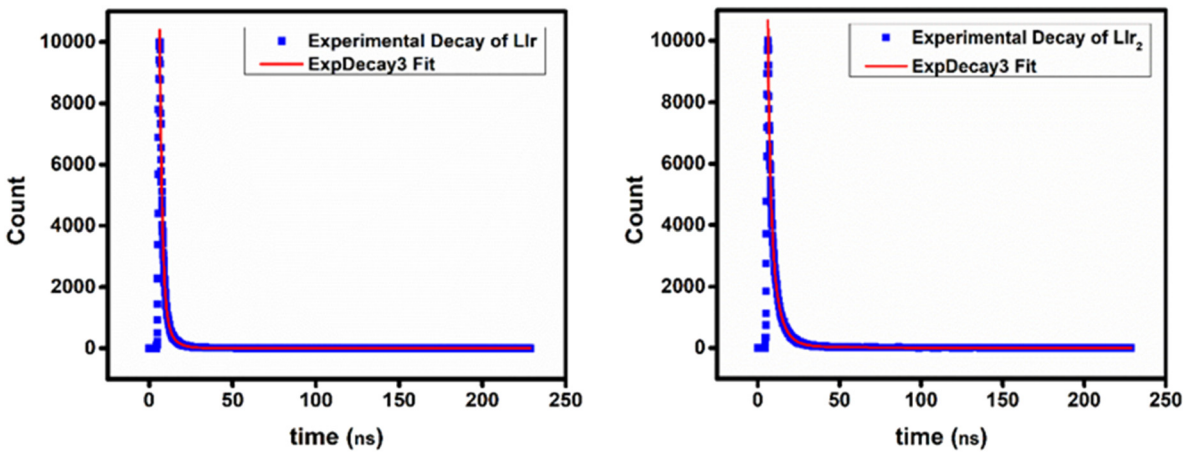

Fig. 3 Lifetime decay plots of 50 μM **LIr** (in CH_3CN) and **LIr$_2$** (in DMSO).

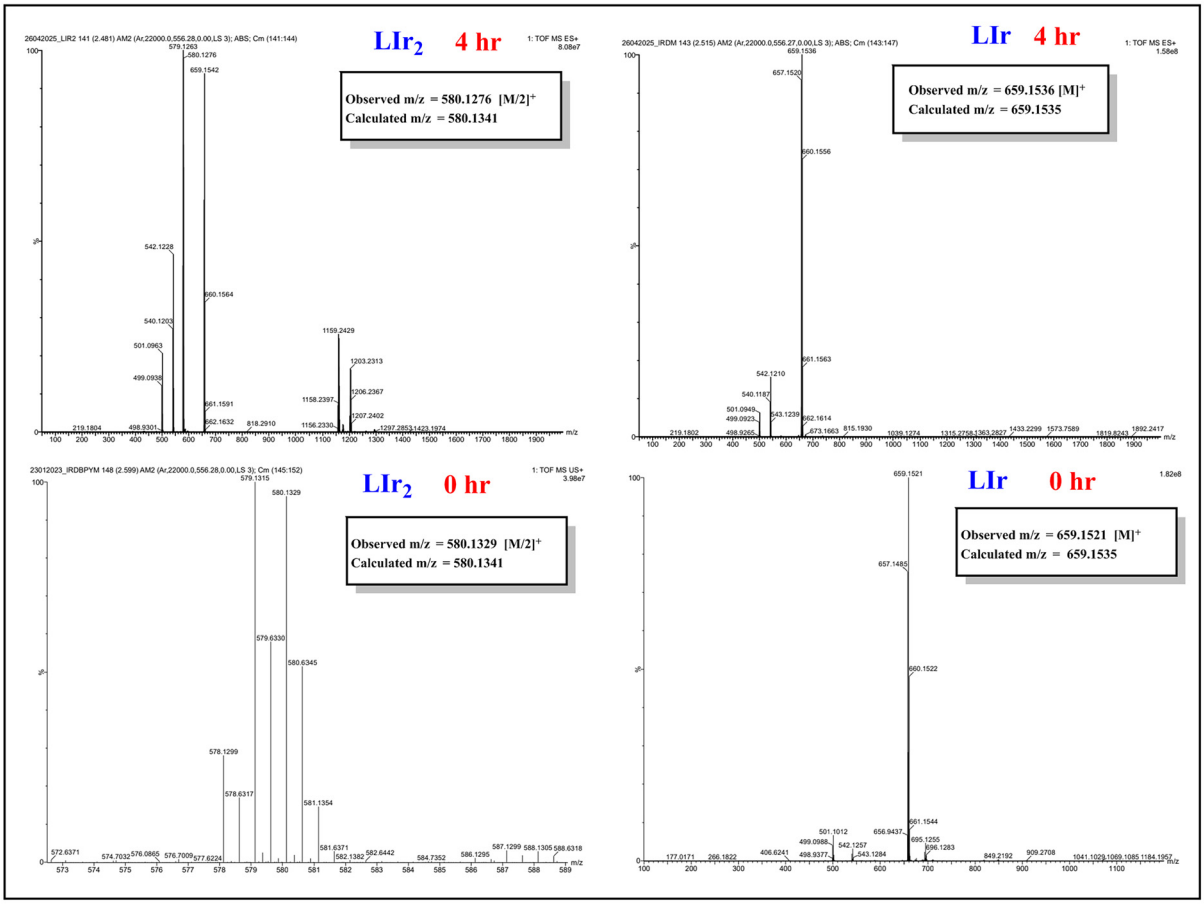

Fig. 4 Photostability study of **LIr** and **LIr$_2$** in 1% DMSO : methanol by HRMS analysis.

Stern–Volmer quenching constant (K_{SV}) (eqn (iv)) was calculated and found to be higher for the bimetallic complex **LIr$_2$** (Fig. S21) (Table 1). The most effective intercalative mode of binding was observed for bimetallic complexes, which may be attributed to the cyclometalated structure. Therefore, the complex **LIr$_2$** may be considered a potential DNA intercalator which may acquire potential anti-cancer activity.

Viscosity measurement

An increase in the specific viscosity of CT-DNA solution was observed after the addition of the metal complex due to the expected DNA intercalation, which separates the base pairs. During this process, the added metal complexes accommodate between CT-DNA base pairs and thereby increase the length of the double helix of CT-DNA. Twisting of the DNA double helix, influenced by the added metal complex, takes place in the case of partial or non-classical binding and thereby alters the optimum length of DNA and its viscosity (eqn (i)). In the case of the synthesized complex **LIr$_2$**, a gradual increase in viscosity was observed, indicating strong intercalation (Fig. S25). Similar experiments were carried out in the case of EtBr and cisplatin using CT-DNA. From the results, it can be concluded that **LIr$_2$** behaves similarly in its interaction with DNA, which suggests an intercalative mode of interaction.

HSA binding study

Human serum albumin (HSA) is a globular protein present in the blood and is synthesized in the liver. This soluble monomeric protein facilitates the transportation of drug molecules through the bloodstream to the cellular membrane. Therefore,

Table 1 Binding constant parameters

Sl. no.	Details	K_b[a] (M^{-1})	K_{SV} (M^{-1})	K_{app} (M^{-1})	K_{HSA} (M^{-1})	K_q (M^{-1} s^{-1})	K (M^{-1})	n
1	**LIr**	0.63×10^4	3.90×10^3	2.6×10^6	0.57×10^5	0.57×10^{13}	5.48×10^4	1.000
2	**LIr$_2$**	1.19×10^4	4.97×10^3	2.6×10^6	0.59×10^5	0.59×10^{13}	0.84×10^4	1.388

[a]DNA binding parameters: K_b = intrinsic binding constant; EtBr quenching studies parameters: K_{SV} = Stern–Volmer constant, K_{app} = apparent binding constant; HSA binding parameters: K_{HSA} = binding constant, K_q = quenching rate constant, n = number of binding sites.

we studied the binding of Ir(III) complexes with HSA to ascertain their facile transportation into the target cells.[22] The changes in fluorescence intensity were recorded after the addition of the complex, and a decreasing trend was observed for both Ir(III) complexes (Fig. S22). HSA binding studies confirmed that this unique behaviour of the complexes may be attributed to both hydrogen bonding and hydrophobic interactions, which contribute to the binding process. From the Stern–Volmer equation (eqn (v)) K_{HSA} of **LIr** and **LIr$_2$** was evaluated to be 0.0575×10^6 M^{-1} and 0.0596×10^6, respectively. From the Scatchard plot, for HSA binding, the value of binding affinity (K) (eqn (vi)) of the complexes **LIr** and **LIr$_2$** was calculated to be 5.48×10^4 M^{-1}, and 0.84×10^4 M^{-1} in DMSO (Fig. S23 and S24) (Table 1). High binding constants indicate the presence of strong interactions between complexes **LIr** and **LIr$_2$** and HSA. Thus, the complexes can cross the biological membrane system. The number of sites (n) which HSA can make accessible to bind the complexes **LIr** and **LIr$_2$** was found to be 1.000 and 1.388, respectively (Table 1).

Singlet oxygen generation study ($^1O_2$)

To rationalize the efficiency of a drug molecule to act as a photosensitizer through the type II pathway in photodynamic therapy, its efficiency to generate singlet oxygen ($^1O_2$) is very crucial. Upon irradiation of light, metal complexes, which act as photosensitizers, are excited to the triplet state through MLCT charge transfer and transfer the energy to the triplet-state molecular oxygen ($^3O_2$), which then relaxes and comes back to the singlet ground state. This energy is utilized for spin pairing, thereby resulting in the generation of highly reactive singlet oxygen ($^1O_2$). Upon exposure to light, a decline in the absorbance peak of DPBF (30 μM) at 425 nm was observed in the presence of the complexes (10 μM), indicating their transformation into 1,2-dibenzoylbenzene (Fig. 5). This study confirmed the generation of singlet oxygen ($^1O_2$), highlighting the role of the complexes as effective photosensitizers. The singlet oxygen quantum yields (Φ_Δ) for complexes **LIr** and **LIr$_2$** were measured to be 0.71 and 0.84 (eqn (vii) and (viii)), respectively, with Rose Bengal (Φ_Δ = 0.76) serving as the reference standard (Fig. S28 and Table 2).

NADH oxidation study

Nicotinamide adenine dinucleotide, also known as NAD^+, is considered one of the main coenzymes which regulates the various redox reactions that occur during the cellular metabolic process. The reduced form of NAD^+ (NADH) plays a crucial role in the mitochondrial electron transport chain (ETC) process.

The ETC system is affected by the oxidation of NADH to NAD^+, thereby hampering the production of energy during the

Table 2 Photocatalytic oxidation study data of NADH with **LIr** and **LIr$_2$**

Details	Φ_Δ	Conditions	TON[a]	TOF (h^{-1})
LIr	0.71	Light	2.1	1.4
		Dark	0.009	0.009
LIr$_2$	0.84	Light	4.02	8.04
		Dark	0.067	0.13

[a]TON = turnover number, TOF = turnover frequency.

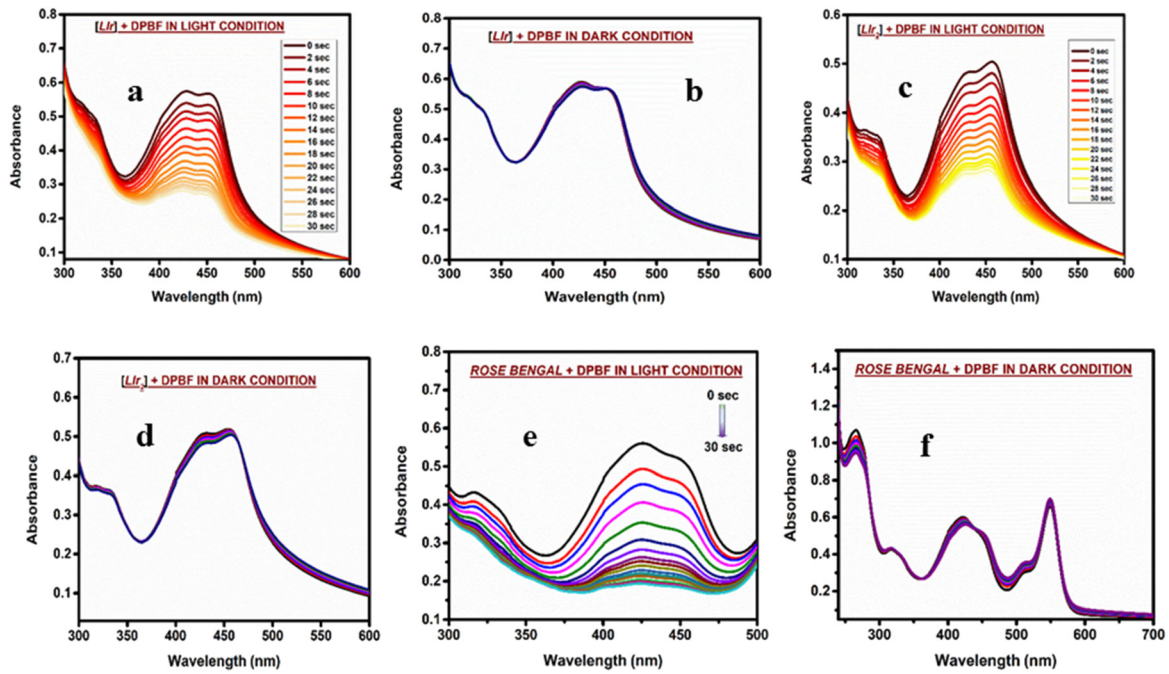

Fig. 5 Singlet oxygen detection study of **LIr** (a) in light and (b) dark conditions; **LIr$_2$** (c) in light and (d) dark conditions; and Rose Bengal (10 μM) (e) in light and (f) dark conditions by DPBF (30 μM).

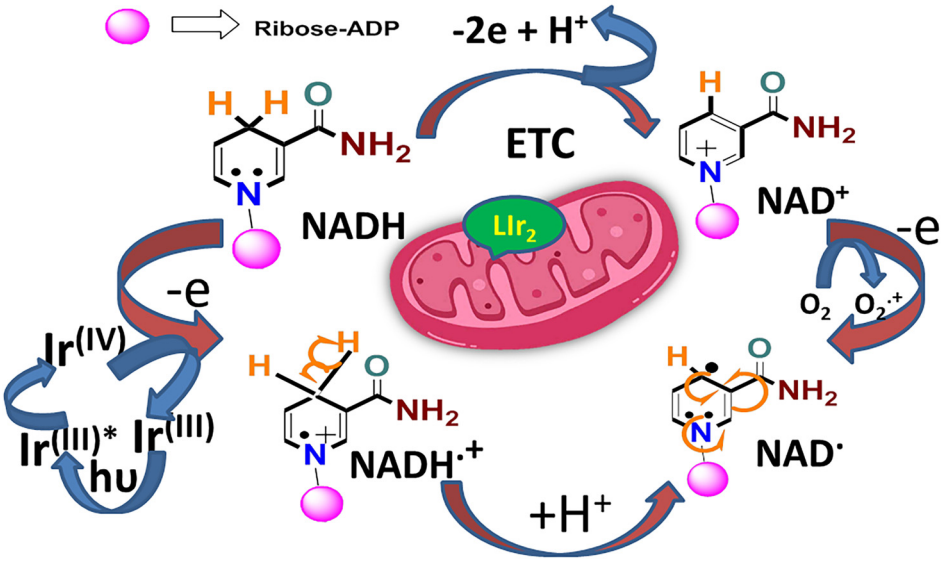

Fig. 6 Plausible mechanism of catalytic oxidation of NADH by the complex.

metabolic process. Fig. 6 shows the plausible representative mechanism for the catalytic photooxidation of NADH by **LIr$_2$**. The photocatalytic activity of the complexes (10 μM) in oxidizing NADH (50 μM) was evaluated by tracking absorbance variations (Fig. 7). NADH absorbs strongly at 340 nm, and its absorbance declines as it is oxidised to NAD^+. Conversely, the absorbance around 260 nm increases, as NAD^+ has higher absorbance at 260 nm compared to NADH. Upon light exposure, a gradual increase in absorbance at 260 nm and a decrease at 340 nm were observed, confirming the oxidation of NADH to NAD^+. The turnover number (TON) for NADH oxidation by **LIr** and **LIr$_2$** under light conditions was 2.1 and 4.02, respectively (Table 2), whereas in the dark, it was significantly lower, with values of 0.009 and 0.067. The turnover frequency (TOF) for **LIr$_2$** was 8.04 h^{-1} with light and 0.13 h^{-1} without light, while for **LIr**, it was 1.4 h^{-1} with light and 0.009 h^{-1} in

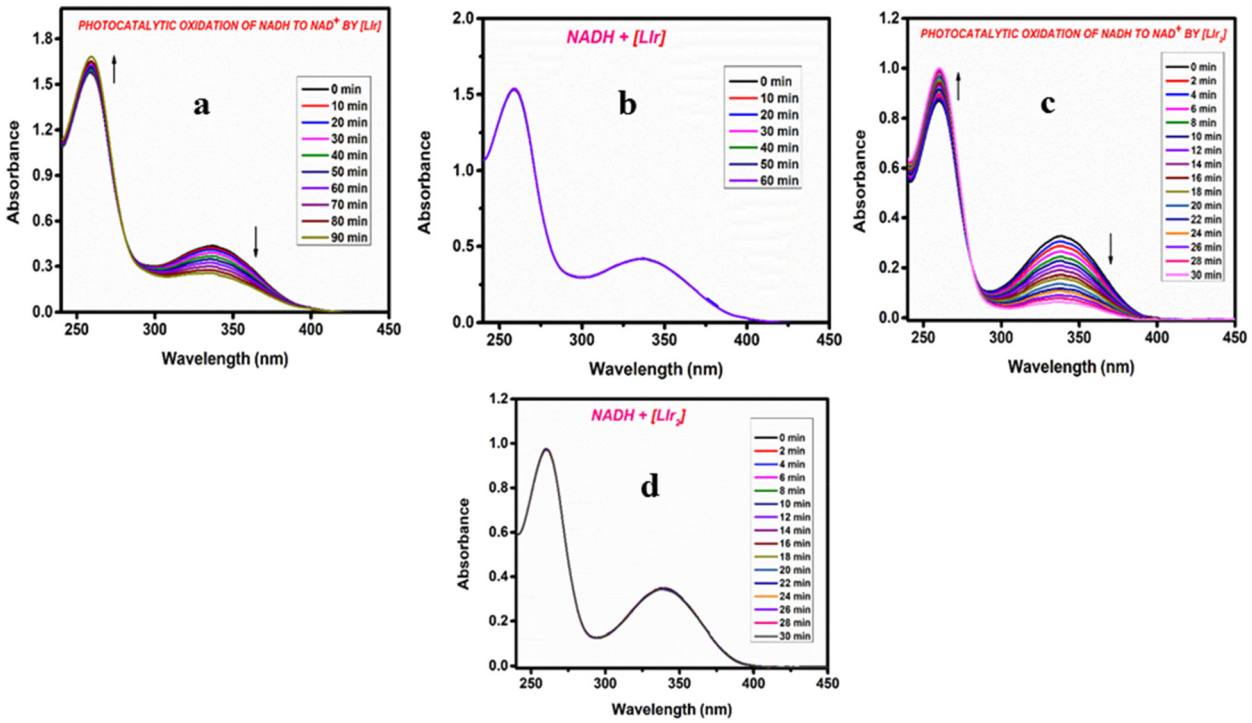

Fig. 7 (a) Photocatalytic oxidation study of NADH (50 μM) with **LIr** (10 μM) and (b) without light irradiation; (c) photocatalytic oxidation study of NADH (50 μM) with **LIr$_2$** (10 μM) and (d) without light.

the dark (eqn (ix)–(xi)). These results confirm that the Ir(III) complexes efficiently generate NAD^+ upon light irradiation, especially complex **LIr$_2$**. This suggests that the high levels of ROS generated by the complexes **LIr** and **LIr$_2$** can disrupt the redox balance by oxidizing NADH. During this oxidation process, the released electrons play a crucial role in generating superoxide radicals ($O_2^{\bullet-}$), which subsequently facilitate the formation of hydrogen peroxide (H_2O_2) from molecular oxygen (O_2).

Methylene blue assay and H_2O_2 generation study

Upon light irradiation, methylene blue dye (3,7-bis(dimethylamino)-phenothiazin-5-ium chloride) undergoes degradation in the presence of hydroxyl ($^\bullet$OH) radicals generated by a photosensitizer.[23] The reduction in absorbance at 654 nm in the methylene blue solution containing 10 μM complex upon light irradiation indicated the generation of hydroxyl radicals (Fig. 8a and b). The degradation efficiency of **LIr$_2$** and **LIr** was determined to be 9.59% and 8.95%, respectively. A plot of $\ln C_0/C$ *vs.* time was analysed for the photocatalytic degradation of methylene blue in the presence of **LIr** and **LIr$_2$**, which follows pseudo-first-order kinetics with rate constants of 0.0016 and 0.0017 min^{-1}, respectively (Fig. S29). Upon light irradiation, these complexes (10 μM) facilitated the generation of H_2O_2 in the presence of NADH (100 μM), as determined using peroxide test strips (Fig. 8c). Complex **LIr$_2$** produced H_2O_2 at a concentration of 1 mg l^{-1}, whereas complex **LIr** showed no detectable color change, indicating the absence of H_2O_2 formation. These results indicate that complex **LIr$_2$** is highly effective for the treatment of hypoxic cancers (type I PDT) as well as under normoxic cellular conditions (type II PDT), whereas complex **LIr** is mostly effective under normoxic cellular conditions.[7]

GSH depletion study

Cancer cells are generally surrounded by a cloud of antioxidants. Therefore, the suppression of these antioxidants by drug molecules is the best pathway to reach the target cancer cells. This can be achieved through a ROS-mediated mechanism. Glutathione, often nicknamed GSH, is one of the major antioxidants present around the cancer cells. It is also proven that cell redox homeostasis is maintained by glutathione. The intracellular depletion method is considered the best pathway to break redox homeostasis, allowing ROS-harvesting metallodrugs to easily attack the cancer cells.[3,7] We have examined the GSH depletion capability of the complexes **LIr** and **LIr$_2$** to analyze the DNA damage *via* a ROS-mediated pathway resulting in cancer cell death. GSH depletion study was carried out using Ellman's reagent (5,5-dithiobis-(2-nitrobenzoic acid)), also known as DTNB, *via* the UV-Vis spectroscopic method. The characteristic peak of DTNB appears at a λ_{max} of ~325 nm. DTNB specifically recognizes the –SH group in any sample. Due to the presence of the –SH group in GSH, when it comes into contact with DTNB, the S–S bond is cleaved and an oxidized adduct (GS-TNB) is formed. As a result, TNB remains free in the solution, and it exhibits λ_{max} ~412 nm. Gradual shifting of the λ_{max} value towards 412 nm from 325 nm indicates the reaction of GSH with DTNB (Fig. 8d). Again, the formation of TNB at a higher rate is indicated by the sharp increase in intensity at λ_{max} 412 nm. A standard curve correlating GSH concentration with absorbance at 412 nm was used to

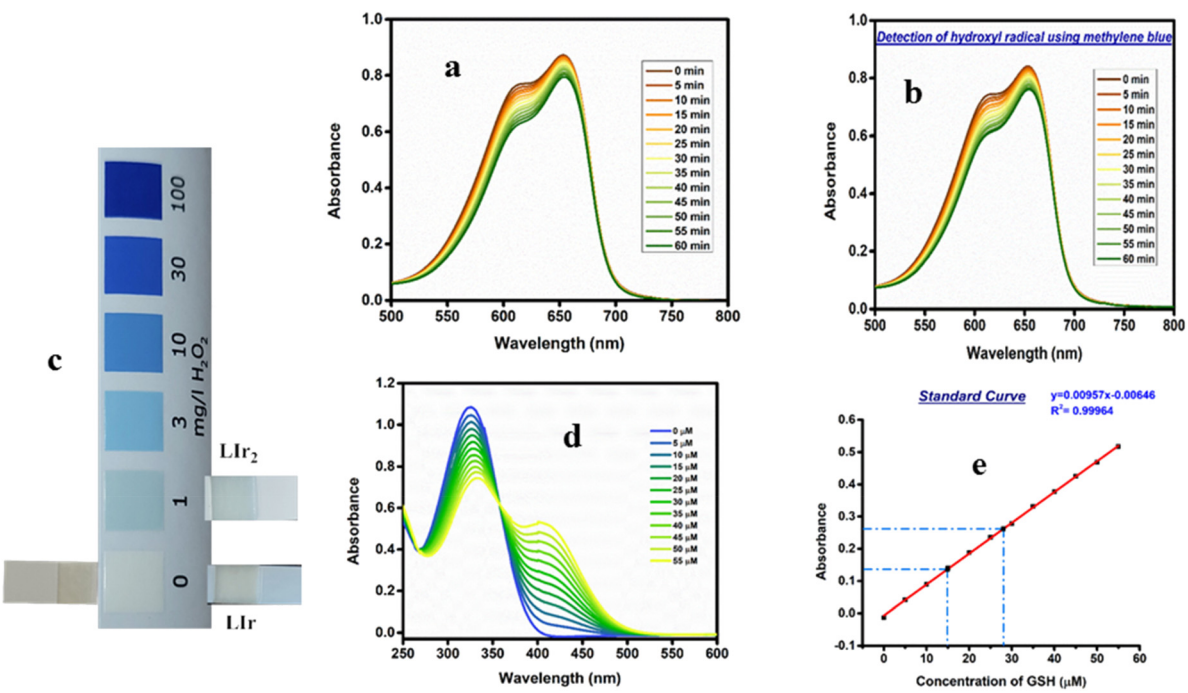

Fig. 8 Detection of hydroxyl radicals of (a) **LIr** and (b) **LIr$_2$** (10 μM); (c) H_2O_2 generation results for 10 μM **LIr** and **LIr$_2$**; (d) UV-vis spectrum of DTNB (55 μM) and GSH (0–55 μM); (e) standard curve plot of GSH concentration *vs.* absorbance at 412 nm for **LIr$_2$** under light conditions.

determine the extent of GSH depletion (Fig. 8e). Upon light irradiation, complex **LIr$_2$** exhibited GSH depletion of 26.97 μM after 10 minutes of irradiation and 40.12 μM after 20 minutes of irradiation, while **LIr** showed a depletion of 2.02 μM after 20 minutes of irradiation. Under dark conditions, following a 5-hour incubation, the GSH depletion for **LIr$_2$** and **LIr** was measured at 7.07 μM and 11.27 μM, respectively (Fig. S30).

In vitro cytotoxicity study

The cytotoxic effect of the complexes **LIr** and **LIr$_2$** was evaluated in the TNBC cell line (MDA-MB-231) under dark and light exposure using the 3-(4,5-dimethylthiazol-2-yl)-2,5-diphenyltetrazolium bromide (MTT) assay. The cells treated with the complex were irradiated with light at a dose of 0–2 J cm^{-2} at an intensity of 4 mW cm^{-2} for about 20 minutes. Complexes **LIr$_2$** and **LIr** demonstrated the minimal dark cytotoxicity, with half-maximal inhibitory concentration (IC_{50}) values of 134.6 ± 1.4 μM and 187.6 ± 1.3 μM, respectively. The complexes **LIr$_2$** and **LIr** showed significant phototoxicity against TNBC, with IC_{50} values of 13.6 ± 0.06 μM (phototoxicity index, PI = 9.9) and 19.5 ± 0.8 μM (PI = 9.6), respectively (Fig. S31).

3. Experimental section

Materials and methods

Highest-grade pure reagents and solvents that were commercially accessible for this experiment were used without further purification. Required chemicals such as iridium(III) chloride, 2,2′-bipyrimidine, L-glutathione reduced (GSH), and deoxyribonucleic acid sodium salt (DNA) were purchased from reputed vendors of Spectrochem, E-Merck, and Sigma-Aldrich Chemical Limited. For recording NMR spectra, tetramethylsilane (TMS) was used as a reference in a 400 MHz high-resolution Bruker DPX spectrometer. For conducting viscosity experiments, an Ostwald viscometer was used. A JASCO V-730 spectrophotometer was used to record UV-visible spectra, with a 1 cm quartz cell. For the measurement of fluorescence, we used a Hitachi F7000 fluorescence spectrophotometer equipped with a xenon lamp. The MDA-MB-231 cell line (TNBC, triple-negative breast cancer) was purchased from the National Centre for Cell Sciences (NCCS), Pune, India. The chemicals used for cell culture work include Dulbecco's Modified Eagle's Medium (DMEM), 1% penicillin, streptomycin, fetal bovine serum, dimethyl sulfoxide (DMSO), and trypsin, which were purchased from Hi-Media Laboratories, Mumbai, India. Consumables required for cell culture work were purchased from Tarson, India. 3-(4,5-Dimethylthiazol-2-yl)-2,5-diphenyltetrazolium bromide (MTT) was purchased from Sigma, India.

Synthesis procedure

Synthesis of iridium precursor [(ppy)Ir(μ-Cl)$_2$]. A total of 120 mg of iridium(III) chloride hydrate was thoroughly dissolved in a mixture of 2-methoxyethanol and water (4 : 1) by stirring for 10 minutes at room temperature. The Ir(III) solution was then added to 128 mg of 2-phenylpyridine solution and allowed to reflux under a nitrogen atmosphere for 24 hours at 110 °C. The progress of the reaction was monitored by TLC.

Yield: 95%; m.p.: >300 °C; R_f (100% methanol): 0.75; ^{1}H NMR (DMSO-d_6, 400 MHz): δ 8.07 (dd, 2H, J_1 = 6.4 Hz, J_2 = 3.6 Hz, ArH), 7.79 (dd, 2H, J_1 = 6.4 Hz, J_2 = 3.6 Hz, ArH), 4.93 (s, 4H, CH_2); ^{13}C NMR (100 MHz, DMSO-d_6): δ 150.9, 143.6, 130.9, 129.7, 30.5; ESI-MS (CH_3OH): calculated m/z = 501.062 $\frac{1}{2}$ [M − Cl]$^+$, observed m/z = 501.0771 $\frac{1}{2}$ [M − Cl]$^+$.

Synthesis of LIr. The Ir(III) precursor (**Ir$_2$Cl$_2$**, 120 mg) was added to a 50 mL R.B. flask containing a methanol : toluene (1 : 4) mixture and stirred continuously for complete dissolution. To this 2,2′-bipyramidine (44 mg, 1 : 1 equivalent) was added, and the mixture was allowed to reflux for 24 hours at 120 °C. The progress of the reaction was monitored by thin-layer chromatography using methanol. After completion of the reaction, the solvent was evaporated with the help of a rotary evaporator, and the obtained product was purified with multiple washings using hexane and diethyl ether.

Yield: 97%; m.p.: 110–115 °C; R_f (100% methanol): 0.62; ^{1}H NMR (DMSO-d_6, 400 MHz): δ 9.32 (dd, J_1 = 2.7 Hz, J_2 = 2.0 Hz, 2H), 8.27 (d, J = 8.0 Hz, 2H), 8.10 (dd, J_1 = 2.2 Hz, J_2 = 3.4 Hz, 2H), 7.93 (m, 8H), 7.15 (t, J = 6.4 Hz, 2H), 7.04 (t, J = 6.8 Hz, 2H), 6.91 (t, J = 6.8 Hz, 2H); ^{13}C NMR (DMSO-d_6, 100 MHz): δ 166.9, 161.9, 160.3, 157.4, 150.5, 148.7, 144.3, 139.6, 131.6, 130.7,126.2, 125.6, 124.5, 123.1, 120.5; IR (KBr, cm^{-1}): ν 3362.53 (Ar C–H stretching), 3066.03 (sp^2 C–H stretching), 2969.66 (sp^3 C–H stretching), 1477.24 (C–H bending), 1401.80 (CH_2 bending), 1245.02 (C–N stretching); ESI-MS (CH_3OH): observed m/z = 659.1521 [M]$^+$, calculated 659.1535 [M]$^+$.

Synthesis of LIr$_2$. **Ir$_2$Cl$_2$** (120 mg) was dissolved in a 1 : 4 mixture of methanol : toluene, followed by the addition of 2,2′-bipyrimidine (19 mg) under reflux condition for 24 hours at 120 °C. Completion of the reaction was monitored by TLC in methanol. The solvent was evaporated with the help of a rotary evaporator, and the obtained crude product was purified with multiple washings using hexane and diethyl ether.

Yield: 92%; m.p.: >300 °C; R_f (methanol): 1.5; ^{1}H NMR (DMSO-d_6, 400 MHz): δ 8.27 (m, 8H), 8.13 (m, 6H), 7.98 (t, J = 15.6 Hz, 4H), 7.92 (d, J = 7.6 Hz, 4H), 7.29 (t, J = 8 Hz, 4H), 7.04 (t, J = 14.8 Hz, 4H), 6.94 (t, J = 14.4 Hz, 4H), 6.13 (d, J = 7.6 Hz, 4H); ^{13}C NMR (DMSO-d_6, 100 MHz): δ 160.2, 158.3, 150.5, 144.3, 139.6, 131.6, 130.7, 130.83, 124.5, 123.1, 120.5; IR (cm^{-1}): ν 3069.29 (sp^2 C–H stretching), 1478.27 (Ar C=C stretching), 1259.26 (C–N stretching), 756.12 (Ar C–H out-of-plane bending); ESI-MS (MeOH): observed m/z = 580.1329 [M]$^{2+}$, calculated m/z = 580.1341 [M]$^{2+}$.

Experimental procedure

UV-Visible study. UV-Visible spectroscopic techniques were applied in different solvents like DMSO, acetonitrile, DCM and methanol to twig the intrinsic photophysical behaviour of the concerned iridium complexes **LIr** and **LIr$_2$** at a concentration of 5 × 10^{-5} mol L^{-1}.

Stability study. The stability of the synthesized complexes was examined in 10% DMSO–PBS, in 1 mM GSH medium and in DMEM medium at 25 °C with the help of UV-Visible spectroscopy.

Solubility and lipophilicity. The potential of metal complexes to shrink tumours depends on the equilibrium between lipophilicity and hydrophilicity. Drug-like characteristics of the metallopharmaceuticals can be well demonstrated by their ability to penetrate lipid bilayer of cell, which is directly related to their lipophilicity. It was found that both Ir complexes, **LIr** and **LIr$_2$**, were highly soluble in DMSO, DMF and decently soluble in water, acetonitrile, methanol, ethanol, but feebly soluble in hydrocarbon solvents. The solubility of these complexes at 25 °C was observed in the range of 6–8 mg ml^{-1} of DMSO–10% DMEM medium (1 : 99 v/v, comparable to cell media). In order to provide insight into lipophilic profile of complexes, we determined the magnitude of *n*-octanol/water partition coefficient ($\log P_{o/w}$, where $P_{o/w}$ = octanol/water partition coefficient) following the conventional shake-flask method. On an orbital shaker, a known quantity of each complex was suspended in water presaturated with *n*-octanol and shaken for 48 hours. The solution was then centrifuged for 10 minutes at 3000 rpm to achieve the phase separation. After the two layers were separated, they were examined using UV-Vis spectroscopy, where the OD of the complexes in octanol and water was used to calculate the partition coefficient ($\log P_{o/w}$) values.

Viscosity study. Viscometric measurements were carried out using an Ostwald viscometer. The concentration of CT-DNA used for experimental studies was 150 μM in nucleotide pairs (NPs). The flow time was recorded using an automatic timer. Each time the sample was analyzed in triplicate and calculated as an average flow time. Data were plotted as $(\eta/\eta_0)^{1/3}$ *vs.* [complex]/[DNA], where η is the viscosity of DNA in the presence of the complex and η_0 is the viscosity of DNA itself. Viscosity values were calculated from eqn (i):

$$\eta = (t - t_0)/t_0 \quad \text{(i)}$$

where t represents the experimental flow time of the DNA-containing solutions and t_0 is the flow time of the buffer alone.

DNA binding study. For DNA binding assay was determined at λ_{max} 260 nm. The molar absorption coefficient, ε_{260}, was taken as 6600 M^{-1} cm^{-1}. Absorption spectral titration was recorded by keeping the complex concentration constant and varying CT-DNA concentration. For titration, each time after adding CT-DNA, the mixture was mixed properly and incubated for 5 min at room temperature. The absorbance value of the complex was then recorded.

The intrinsic DNA binding constant (K_b) was calculated using eqn (ii):

$$\frac{[\text{DNA}]}{(\varepsilon_a - \varepsilon_f)} = \frac{[\text{DNA}]}{(\varepsilon_b - \varepsilon_f)} + \frac{1}{K_b(\varepsilon_a - \varepsilon_f)} \quad \text{(ii)}$$

where, [DNA] = DNA concentration in the base pairs, ε_a = apparent extinction coefficient, ε_b = fully bound extinction coefficient of the complex with DNA and ε_f = the free-from extinction coefficient of the complex. A plot of [DNA]/($\varepsilon_a - \varepsilon_f$) *vs.* [DNA] was constructed. The value of the binding constant (K_b) was calculated from the ratio of the slope to intercept.

Ethidium bromide displacement assay

The K_{app} value was calculated from eqn (iii):

$$K_{app} \times [\text{complex}]_{50} = K_{EtBr} \times [\text{EtBr}] \quad \text{(iii)}$$

where, K_{EtBr} = binding constant of EtBr, and [EtBr] = 8×10^{-6} M.

Stern–Volmer equation was used for the determination of the Stern–Volmer quenching constant (K_{SV}). A linear plot of I_0/I *vs.* [complex] was plotted. The K_{SV} value was calculated using eqn (iv):

$$\frac{I_0}{I} = 1 + K_{SV}[\text{Q}], \quad \text{(iv)}$$

where I_0 = fluorescence intensity in the absence of complex, I = fluorescence intensity in the presence of complex, and [Q] = concentration.

HSA binding study. Linear plot of I_0/I *vs.* [complex] was obtained using eqn (v):

$$\frac{I_0}{I} = 1 + K_{HSA}[\text{Q}] = 1 + k_q\tau_0[\text{Q}] \quad \text{(v)}$$

where I_0 = fluorescence intensity of HSA in the absence of the complex, I = the fluorescence intensity of HSA in the presence of the complex, τ_0 = lifetime of tryptophan in HSA and k_q = bimolecular quenching constant.

The Scatchard equation gives the binding properties of the complexes, which are shown below (eqn (vi)):

$$\log\left(\frac{I_0 - I}{I}\right) = \log K + n \log[\text{Q}] \quad \text{(vi)}$$

where K = binding constant and n = the number of binding sites.

Photoinduced singlet oxygen generation

The effectiveness of **LIr** and **LIr$_2$** in the generation of singlet oxygen under the photosensitized conditions was measured using the 1,3-diphenylisobenzofuran (DPBF) assay with the help of a UV-Vis spectrophotometer. In this study, the highly reactive diene DPBF was used as a fluorescent probe and Rose Bengal (RB) as a standard singlet oxygen generator. The photooxidation of DPBF was monitored from 0 s to 30 s. The $^1O_2$ quantum yield was calculated by comparing the quantum yield of photooxidation of DPBF after sensitization by Rose Bengal (RB) ($\Phi[^1O_2]$ = 0.76 in DMSO) as a reference compound according to eqn (vii):

$$\Phi_\Delta c = \Phi_{\Delta RB} \times m_c/m_{RB} \times F_{RB}/F_c \quad \text{(vii)}$$

where *c* signifies complex, and RB represents Rose Bengal. Φ_Δ is the quantum yield of $^1O_2$, and m is the slope of the plot of DPBF absorbance at 425 nm *vs.* irradiation time. F is the absorption correction factor, which is given by eqn (viii):

$$F = 1 - 10^{-OD} \quad \text{(viii)}$$

where, OD is the optical density at the irradiation wavelength.

NADH/NADPH oxidation

The oxidation of NADH/NADPH (50 μM) in DMSO–PBS solution was monitored by UV-Vis spectroscopy following the titration method upon gradual addition of the complex at a concentration of 10 μM at ambient temperature under both dark and light conditions. The turnover number of the catalytic process was calculated using eqn (ix)–(xi):

$$[NAD^+] = [(Abs_{340\ nm})_{initial} - (Abs_{340\ nm})_{final}] \times [NADH] \quad (ix)$$

$$\text{Turn over number (TON)} = [NAD^+]/[\text{catalyst}] \quad (x)$$

$$\text{Turnover frequency (TOF)} = \text{turnover number/time } (h^{-1}). \quad (xi)$$

Cell viability assay

Briefly, MDA-MB-231 (TNBC) cells were maintained in Dulbecco's Modified Eagle's Medium (DMEM) supplemented with 10% fetal bovine serum (FBS), and incubated at 5% CO_2 and 37 °C. Once MDA-MB-231 cells reached 80–90% confluency, they were trypsinised and seeded for further experiments. To determine the cytotoxic effects of the compounds, MDA-MB-231 cells were seeded in a 96-well plate for 24 hours and treated with the test compounds (**LIr**, **LIr$_2$** dissolved in 0.1% DMSO, and further diluted in DMEM medium) at 200–6.25 μM concentrations under both light and dark conditions, then incubated for 24 hours. After treatment, the MTT was added and incubated for 4 hours, followed by adding DMSO to solubilise formazan crystals. The cell viability was measured at an absorbance of 570 nm using a microplate reader (Bio-Tek, USA). The IC_{50} concentrations of the compounds were used for further experiments.

4. Conclusion

Thus, it can be concluded that we successfully designed, synthesized, and characterized 2,2′-bipyrimidine-based cyclometalated Ir(III) complexes, capable of depleting GSH and generating ROS. The HSA and DNA binding studies prove their potency towards biomolecular interactions. Based on the results obtained from various studies performed, we can propose that although type I and type II PDT pathways are possible for both the complexes, the bimetallic complex **LIr$_2$** is effective for both normoxic (type II) and hypoxic (type I) tumours, whereas the monometallic complex **LIr** is effective only for normoxic cells. Thus, the cancer cell death can be triggered by both pathways, which enhances the efficacy of the complex as a phototherapeutic agent. The complex **LIr$_2$** exhibited enhanced phototoxicity against TNBC cell line MDA-MB-231 (PI = 9.9) compared to **LIr** (PI = 9.6), making it ideal for PDT. Collectively, these findings show that the 2,2′-bipyrimidine-based cyclometalated Ir(III) complexes exhibit efficacy as promising PDT agents.

Conflicts of interest

There are no conflicts to declare.

Data availability

The data supporting this article have been included as part of the SI. Supplementary information is available. See DOI: https://doi.org/10.1039/d5dt01164g.

CCDC 2446109 contains the supplementary crystallographic data for this paper.[24]

Acknowledgements

The authors express gratitude to the Department of Science and Technology, Government of India, for their support in this research through the DST-SERB CRG project grant (CRG/2021/002267). Additionally, the authors appreciate the Vellore Institute of Technology for facilitating VIT SEED funding. This work was financially supported by Vellore Institute of Technology (VIT), Vellore under the Faculty Seed Grant (RGEMS) (Sanction Order No. SG20220001). Recognition is also extended to DST, New Delhi, India, for the DST-FIST project. The authors acknowledge the Sophisticated Analytical Instruments Facility (SAIF), IIT Madras, for providing access to the fluorescence lifetime measurement system.

References

1 C. Gonzalo-Navarro, E. Zafon, J. A. Organero, F. A. Jalón, J. C. Lima, G. Espino, A. M. Rodríguez, L. Santos, A. J. Moro, S. Barrabés, J. Castro, J. Camacho-Aguayo, A. Massaguer, B. R. Manzano and G. Durá, *J. Med. Chem.*, 2024, **67**, 1783–1811.
2 Y. Yang, Y. Gao, J. Zhao and S. Gou, *Inorg. Chem. Front.*, 2024, **11**, 436–450.
3 X. Cui, J. Zhao, Z. Mohmood and C. Zhang, *Chem. Rec.*, 2016, **16**, 173–188.
4 L. Z. Zeng, X. L. Li, Y. A. Deng, R. Y. Zhao, R. Song, Y. F. Yan, M. F. Wang, X. H. Wang, X. Ren and F. Gao, *Inorg. Chem.*, 2025, **64**, 967–977.
5 S. U, U. Basu and P. Paira, *ChemMedChem*, 2024, **20**, e202400649.
6 P. W. Zabierowski, O. Jeannin, T. Fix, J. F. Guillemoles, L. J. Charbonnière and A. M. Nonat, *Inorg. Chem.*, 2021, **60**, 8304–8314.
7 J. Martínez-Lillo, D. Armentano, G. De Munno, J. Cano, F. Lloret, M. Julve and J. Faus, *Inorg. Chem.*, 2011, **50**, 12405–12407.
8 N. Suryadevara, M. J. Giansiracusa, R. W. Gable and C. Boskovic, *Cryst. Growth Des.*, 2025, **25**, 4940–4949.
9 N. Roy, T. Dasgupta, S. Ghosh, M. Jayaprakash, M. Pal, S. Shanavas, S. K. Pal, V. Muthukumar, A. Senthil Kumar,

R. Tamizhselvi, M. Roy, B. Bose, D. Panda, R. Chakrabarty and P. Paira, *Langmuir*, 2024, **40**, 25390–25404.
10 D. Tang, M. Cui, B. Wang, C. Xu, Z. Cao, J. Guo, H. Xiao and K. Shang, *Adv. Mater.*, 2024, **36**, 2406815.
11 Z. Liu, I. Romero-Canelón, A. Habtemariam, G. J. Clarkson and P. J. Sadler, *Organometallics*, 2014, **33**, 5324–5333.
12 A. Burguete, E. Pontiki, D. Hadjipavlou-Litina, R. Villar, E. Vicente, B. Solano, S. Ancizu, S. Pérez-Silanes, I. Aldana and A. Monge, *Bioorg. Med. Chem. Lett.*, 2007, **17**, 6439–6443.
13 J. P. Dirlam, J. E. Presslitz and B. J. Williams, *J. Med. Chem.*, 1983, **26**, 1122–1126.
14 S. Ghosh and P. Paira, *Eur. J. Inorg. Chem.*, 2025, e202400769.
15 P. Štarha, *Inorg. Chem. Front.*, 2025, **12**, 897–954.
16 Y. Niu, S. Tang, J. Li, C. Huang, Y. Yang, L. Zhou, Y. Liu and X. Zeng, *J. Inorg. Biochem.*, 2025, **264**, 112808.
17 R. Das and P. Paira, *Dalton Trans.*, 2023, **52**, 15365–15376.
18 K. A. King and R. J. Watts, *J. Am. Chem. Soc.*, 1987, **109**, 1589–1590.
19 H. Fu, S. Wang, Y. Gong, H. Dong, K. Lai, Z. Yang, C. Fan, Z. Liu and L. Guo, *Bioorg. Chem.*, 2025, **155**, 108148.
20 P. Li, L. Guo, J. Li, Z. Yang, H. Fu, K. Lai, H. Dong, C. Fan and Z. Liu, *Dalton Trans.*, 2024, **53**, 1977–1988.
21 S. C. Marker, S. N. MacMillan, W. R. Zipfel, Z. Li, P. C. Ford and J. J. Wilson, *Inorg. Chem.*, 2018, **57**, 1311–1331.
22 N. Wu, T. Liu, M. Tian, C. Liu, S. Ma, H. Cao, H. Bian, L. Wang, Y. Feng and Q. I. Jianni, *Mol. Med. Rep.*, 2023, **29**, 24.
23 I. Khan, K. Saeed, I. Zekker, B. Zhang, A. H. Hendi, A. Ahmad, S. Ahmad, N. Zada, H. Ahmad, L. A. Shah, T. Shah and I. Khan, *Water*, 2022, **14**, 242.
24 S. U, R. Das, I. P. Latha Laxmi, N. Roy, R. Roy, L. Mathivathanan, T. Ramasamy, R. Chakrabarty and P. Paira, CCDC 2446109, Experimental Crystal Structure Determination, 2025, DOI: **10.5517/ccdc.csd.cc2n3crx**.